RSC Advances

PAPER

View Article Online
View Journal | View Issue



Cite this: *RSC Adv.*, 2017, **7**, 19181

# $Co_9S_8$@N,P-doped porous carbon electrocatalyst using biomass-derived carbon nanodots as a precursor for overall water splitting in alkaline media†

Rongrong Liu,[ab] Haimin Zhang,[*a] Xian Zhang,[ab] Tianxing Wu,[a] Huijun Zhao[ac] and Guozhong Wang[*a]

In this study, we first synthesized $Co_9S_8$@N-doped porous carbon ($Co_9S_8$@NC) using shrimp-shell derived carbon nanodots as a carbon/nitrogen source in the presence of $CoSO_4$ by a one-step molten-salt calcination method. This was followed by low-temperature phosphorization in the presence of $NaH_2PO_2$, whereby $Co_9S_8$@N,P-doped porous carbon ($Co_9S_8$@NPC) was finally obtained using the $Co_9S_8$@NC as a precursor. The results demonstrated that the molten-salt calcination approach can effectively create a pyrolytic product with a porous structure and improve the material's surface area, which is favourable for electrocatalysis-related mass transport and the exposure of catalytic active sites during electrocatalysis. As an electrocatalyst, $Co_9S_8$@NPC exhibits higher catalytic activity for the hydrogen evolution reaction (HER) than $Co_9S_8$@NC in an alkaline medium. Among all the investigated $Co_9S_8$@NPC catalysts, $Co_9S_8$@NPC-10 (mass ratio of $NaH_2PO_2$ to $Co_9S_8$@NC = 10 : 1) displays the best HER activity with an overpotential of 261 mV at 10 mA $cm^{-2}$ in the alkaline medium. Interestingly, $Co_9S_8$@NPC-10 also displays good catalytic activity for the oxygen evolution reaction (OER) in this study. Owing to its bifunctional catalytic activity towards the HER and OER, the fabricated $Co_9S_8$@NPC-10 was simultaneously used as an anode and cathode material to generate $O_2$ and $H_2$ from overall water splitting in the alkaline medium, exhibiting a nearly 100% faradaic yield. This study would be helpful to the design and development of high performance non-precious metal electrocatalysts to be applied in overall water splitting to produce $H_2$ and $O_2$.

Received 13th February 2017
Accepted 14th March 2017

DOI: 10.1039/c7ra01798g

rsc.li/rsc-advances



## Introduction

Electrocatalytic water splitting has been widely regarded as a potential renewable and sustainable energy technology to generate $H_2$ for replacing traditional fossil fuels, and $H_2$ has a high energy density and an environmentally-friendly combustion product.[1–3] To drive electrocatalytic water splitting to generate $H_2$, an active electrocatalyst for the hydrogen evolution reaction (HER) is critically important, which would reduce the overpotential for the HER, thereby making the whole water splitting process more energy efficient. To date, the most efficient HER electrocatalysts are almost exclusively applied in acidic media owing to the rapid reaction rate of $H^+$ to $H_2$ on the catalyst surface,[4–8] however, studies on HER catalysts in alkaline media are relatively rare due to the more complex reaction mechanism of $OH^-$ on the catalyst surface and the sluggish kinetics of the counterpart electrode reaction for the oxygen evolution reaction (OER) during electrocatalytic water splitting.[9–11] So far, Pt-based and Ru/Ir-based catalysts have been extensively considered as the most active electrocatalysts for the HER and OER respectively in alkaline media, however, their high costs and source scarcity have limited large-scale production applications.[3,7,12–14] Therefore, searching for cheap, earth-abundant and efficient electrocatalysts with high HER and OER activities is still highly desirable.

Up to now, a variety of materials with different structures and compositions have been developed as electrocatalysts for electrocatalytic water splitting to generate $H_2$ in alkaline media.[15–20] Among them, transition metal sulfides such as molybdic sulfide,[21–23] nickel sulfide,[24–26] iron sulfide[27] and cobalt sulfide[28,29] have attracted considerable interest due to their

[a]*Key Laboratory of Materials Physics, Centre for Environmental and Energy Nanomaterials, Anhui Key Laboratory of Nanomaterials and Nanotechnology, CAS Center for Excellence in Nanoscience, Institute of Solid State Physics, Chinese Academy of Sciences, Hefei 230031, China. E-mail: zhanghm@issp.ac.cn; gzhwang@issp.ac.cn; Tel: +86 551 65591973*

[b]*University of Science and Technology of China, Hefei 230026, China*

[c]*Centre for Clean Environment and Energy, Griffith University, Gold Coast Campus, QLD 4222, Australia*

† Electronic supplementary information (ESI) available: SEM image of $Co_9S_8$@NPC-10 without NaCl–KCl, $N_2$ adsorption–desorption isotherm and pore size distribution curve of $Co_9S_8$@NPC-10 without NaCl–KCl, and electrocatalytic measurement results. See DOI: 10.1039/c7ra01798g

earth abundance and high electrocatalytic activity. However, the poor conductivities of the transition metal sulfides have limited their overall electrocatalytic performance, so they are always considered for loading on conductive substrates to improve the materials' electrical conductivity.[20,30–34] Compared to other conductive substrates, heteroatom (*e.g.*, N, S, P *etc.*) doped/co-doped carbonaceous materials have aroused wide attention because of their prominent conductivity and additive electrocatalytic activity. However, the most highly-efficient transition metal sulfide@carbon catalysts with HER activity are almost exclusively synthesized using chemical reagents as the carbon and heteroatom sources, undoubtedly enhancing the catalysts' cost and synthetic complexity.[35] In our previous studies, raw biomass (*e.g.*, shrimp shell) derived N-doped carbon nanodots have been used as a carbon and nitrogen source when assembling and fabricating high performance carbon-based electrocatalysts, which exhibit superior electrocatalytic activities and have potential applications as air cathode materials in Zn-air batteries.[10,36] Furthermore, developing a simple approach to fabricate transition metal sulfide@heteroatom-doped carbon catalysts with improved HER activity using biomass-derived N-doped carbon nanodots as the carbon and nitrogen source should be very feasible, and this material would effectively and efficiently perform electrocatalytic water splitting to produce $H_2$.

In this study, we first synthesize $Co_9S_8$@N-doped porous carbon ($Co_9S_8$@NC) using shrimp-shell derived carbon nanodots as the carbon/nitrogen source in the presence of $CoSO_4$ by a one-step molten-salt calcination method. The molten-salt assisted approach has been widely employed to fabricate carbon-based materials with porous structures in order to improve their surface areas, enhancing electrocatalysis-related mass transport and the exposure of catalytic active sites when they are used as electrocatalysts.[37,38] The resulting $Co_9S_8$@NC electrocatalyst exhibits HER activity in an alkaline medium, and this HER activity is dramatically improved by the further phosphorization treatment of $Co_9S_8$@NC to obtain $Co_9S_8$@N,P-doped porous carbon ($Co_9S_8$@NPC). The results demonstrate that the appropriate P doping content in $Co_9S_8$@NC is paramount for high HER activity in alkaline media. Simultaneously, it is also found that $Co_9S_8$@NC before and after P doping exhibits similar OER activity in the alkaline medium. This $Co_9S_8$@NPC with bifunctional catalytic activity towards the HER and OER, used concurrently as an anode and cathode material, displays $O_2$ and $H_2$ generation efficiencies of 6.6 and 13.4 μmol $min^{-1}$, respectively, and nearly 100% faradaic efficiency in the alkaline medium.

# Experimental section

### Synthesis of N-doped carbon nanodots

N-doped carbon nanodots were synthesized using shrimp shells as the starting material by a simple hydrothermal method as reported in our previous study.[39] In a typical synthesis, 3.0 g of dried shrimp shell was first ground to a powder and added to 50 mL of deionized water, and then the mixture was transferred to a 100 mL Teflon-lined autoclave. The hydrothermal reaction was performed at 180 °C for 15 h. After that, the obtained solution was filtrated with a 0.2 μm cellulose membrane to remove large particles. The rest of the supernatant was concentrated at 80 °C and the concentration of the resulting N-doped carbon nanodot solution was around 50 mg $mL^{-1}$.

### Synthesis of $Co_9S_8$@NC and $Co_9S_8$@NPC

Utilizing shrimp shell derived N-doped carbon nanodots as a carbon and nitrogen source, $Co_9S_8$@N-doped porous carbon ($Co_9S_8$@NC) was fabricated by a one-step molten-salt calcination method (with a mole ratio of KCl to NaCl of 1 : 1) in the presence of $CoSO_4 \cdot 7H_2O$. In a typical procedure, 10 mL of 50 mg $mL^{-1}$ N-doped carbon nanodot solution, 0.1 g $CoSO_4 \cdot 7H_2O$ and 6.0 g KCl–NaCl were mixed by stirring until a homogeneous solution was obtained, and then the above mixture was dried at 80 °C for 6 h. Subsequently, the obtained solid mixture was firstly heated to 400 °C for 2 h at a temperature rising rate of 2 °C $min^{-1}$, and then the pyrolysis temperature was further increased to 900 °C at a temperature rising rate of 5 °C $min^{-1}$ for 2 h in a $N_2$ atmosphere. The pyrolytic product was subsequently immersed in 1.0 M HCl solution overnight to remove non-active components and then adequately washed with deionized water. Finally, the sample was dried at 80 °C for further characterization and use. To obtain $Co_9S_8$@N,P-doped porous carbon ($Co_9S_8$@NPC), 20 mg of $Co_9S_8$@NC and 200 mg of $NaH_2PO_2 \cdot H_2O$ were placed in two separate positions in a corundum porcelain boat. The samples were heated to 400 °C for 2 h in a $N_2$ atmosphere. With the same fabrication method, different mass ratios of $NaH_2PO_2 \cdot H_2O$ to $Co_9S_8$@NC were investigated in this study to obtain $Co_9S_8$@NPC samples with different P doping amounts. The obtained products were denoted as $Co_9S_8$@NPC-*X* (where *X* represents the mass ratio of $NaH_2PO_2 \cdot H_2O$ to $Co_9S_8$@NC).

### Characterization

Powder X-ray diffraction (XRD) patterns of the samples were recorded on a Philips X-Pert Pro X-ray diffractometer with Cu Kα radiation ($\lambda_{K\alpha_1}$ = 1.5418 Å). Field emission scanning electron microscope (FESEM) images of the samples were taken on an FESEM (Quanta 200FEG) operated at an acceleration voltage of 10.0 kV. Transmission electron microscope (TEM) images of the samples were obtained with a high resolution TEM (JEOL 2010), operated at an acceleration voltage of 200 kV. Raman spectra of the samples were recorded on a LabRAM HR800 confocal microscope Raman system (Horiba Jobin Yvon) using an Ar ion laser operating at 632 nm. X-ray photoelectron spectroscopy (XPS) analysis was performed on an ESCALAB 250 X-ray photoelectron spectrometer (Thermo, America) equipped with an Al $K\alpha_{1,2}$ X-ray source producing monochromatized radiation at 1486.6 eV. The surface areas and porosities of the samples were measured with a Surface Area and Porosity Analyzer (Tristar 3020M).

### Electrochemical measurements

All the electrochemical measurements were performed on an electrochemical workstation (CHI 660E, CH Instruments, Inc.,

 

Shanghai, China) and a PINE rotating disk electrode (RDE) system (Pine Instruments Co. Ltd. USA) in a conventional three-electrode cell. A catalyst coated glassy carbon (GC) electrode with a diameter of 5.0 mm, Ag/AgCl (saturated KCl), and platinum wire were used as the working electrode, reference electrode and counter electrode, respectively. All the potentials measured in this study were converted into potentials *versus* the reversible hydrogen electrode (RHE) according to the equation: $E_{vs.\ RHE} = E_{vs.\ Ag/AgCl} + E^{o}_{Ag/AgCl} + 0.059$ pH, where the value of $E^{o}_{Ag/AgCl}$ was −0.197 V *vs.* RHE.

The electrolyte was a 1.0 M KOH solution prepared with deionized water. Prior to the measurements, a GC electrode was polished carefully with 5.0, 0.3 and 0.05 μm alumina slurry, and then ultrasonically cleaned in water and absolute ethanol to remove residues. To prepare each catalyst ink, the catalyst (4.0 mg) was mixed with 950 μL of ethanol and 50 μL of 5.0 wt% Nafion solution under sonication for 30 min. To prepare each catalyst coated GC electrode, 20 μL of the catalyst ink was cast onto the cleaned GC electrode surface, which was then dried at room temperature. For the HER test, the polarization curves were obtained by sweeping the potential from 0.1 to −0.8 V (*vs.* RHE) at a potential sweep rate of 5.0 mV $s^{-1}$. And for the OER test, the polarization curves were recorded at 1.1 to 1.8 V (*vs.* RHE) at a potential sweep rate of 10 mV $s^{-1}$. Electrochemical impedance spectroscopy (EIS) was carried out with an amplitude of 5.0 mV and a frequency range from 100 kHz to 0.1 Hz. The stability test was performed in 1.0 M KOH solution at room temperature with the potential cycling between +0.2 and −0.3 V (*vs.* RHE) at a sweep rate of 50 mV $s^{-1}$ for 2000 cycles. The overall water splitting reaction was performed in a two-electrode system using $Co_9S_8$@NPC coated carbon cloths as the anode and cathode in 1.0 M KOH solution with a simple drainage method to collect $H_2$ and $O_2$. In general, 0.5 mL of the above prepared catalyst ink was coated on a carbon cloth with an area of 2.0 $cm^2$ for each electrode (a catalyst loading amount of 1.0 mg $cm^{-2}$).

## Results and discussion

In our previous studies, shrimp-shell derived N-doped carbon nanodots were used as a carbon and nitrogen source to fabricate N-doped carbon-based electrocatalysts, which exhibited superior electrocatalytic activities and potential applications in Zn-air batteries and in water splitting to generate $H_2/O_2$.[10,36] In this study, $Co_9S_8$@N,P-doped porous carbon ($Co_9S_8$@NPC) was obtained by a simple molten-salt (NaCl–KCl) calcination method in the presence of $CoSO_4$, followed by low-temperature phosphorization in the presence of $NaH_2PO_2$. Obviously, $Co_9S_8$@NPC is mainly composed of interconnected nanosheets with a porous structure (Fig. 1A and inset, taking $Co_9S_8$@NPC-10 as an example). This porous structure of $Co_9S_8$@NPC may be due to the molten-salt assisted pyrolysis approach, and no porous structure can be observed without the addition of NaCl–KCl during pyrolysis (Fig. S1A, ESI†). The porous structure of $Co_9S_8$@NPC can effectively improve the material's surface area, which is favourable for enhancing electrocatalysis-related mass transport and the exposure of catalytic active sites when it is used as an electrocatalyst.[6,39] Detailed structure information was further obtained by TEM characterization. As shown in Fig. 1B, irregular nanoparticles loaded on a thin carbon nanosheet can be clearly observed, and a high-resolution TEM image (inset in Fig. 1B) shows lattice fringes with a *d* spacing of 0.30 nm, corresponding to the (311) plane of $Co_9S_8$.[29] To further confirm the composition and element distribution of $Co_9S_8$@NPC-10, elemental mapping analysis was performed. Accordingly, the elemental mapping images (Fig. 1C) show that $Co_9S_8$@NPC-10 is mainly composed of C, O, P, S and Co, and moreover, that Co and S are uniformly overlaid and P is homogenously distributed on the entire carbon structure. The above results suggest the formation of $Co_9S_8$ and P doping in the carbon nanosheets after molten-salt calcination and low-temperature phosphorization. $Co_9S_8$ and a P dopant in carbon structures have been proven to be active species to create catalytic active sites for improving catalysts' activities.[40,41] In elemental mapping analysis, the element N was not detected, possibly owing to its low doping content in $Co_9S_8$@NPC-10, which can be further confirmed by the following high resolution XPS analysis.

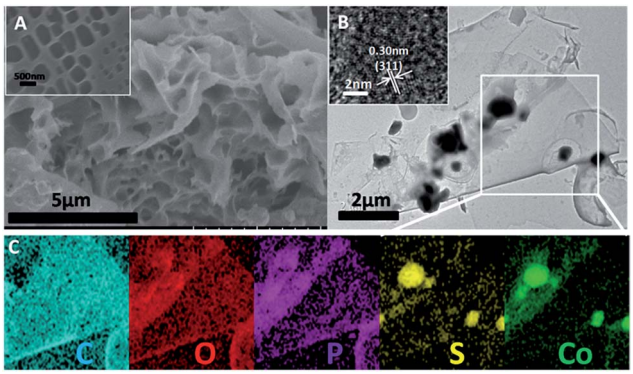


Fig. 1 (A) and (B) SEM and TEM images of $Co_9S_8$@NPC-10. The insets in (A) and (B) are the corresponding high magnification SEM and high resolution TEM images. (C) Corresponding elemental mapping analysis of the selected area from (B).

The X-ray diffraction (XRD) technique was used to confirm the crystalline phase of the as-synthesized samples. Fig. 2A shows the XRD patterns of $Co_9S_8$@NC and $Co_9S_8$@NPC samples. As shown, $Co_9S_8$@NC without phosphorization exhibits diffraction peaks at $2\theta = 15.4°$, 29.8°, 31.2°, 47.5° and 52.0°, which are assigned to the (111), (311), (222), (511) and (440) planes, respectively, of cubic $Co_9S_8$ (PDF#65-6801).[29,35,42,43] The weak diffraction peak at $2\theta = 24.7°$ can be indexed to graphitic carbon.[39,44] After phosphorization, similar diffraction peaks can be observed for $Co_9S_8$@NPC-5, $Co_9S_8$@NPC-10 and $Co_9S_8$@NPC-15, and moreover, no new diffraction peaks from $CoP_x$ are detected in the XRD patterns of any of the samples, indicating no significant effect of phosphorization on the $Co_9S_8$ crystal phase, and suggesting possible P doping in the graphitic carbon structure that was previously obtained by the pyrolysis of the shrimp-shell derived N-doped carbon nanodots. Raman spectroscopy is an efficient tool to investigate the level of defects in carbon materials. We therefore determined the Raman

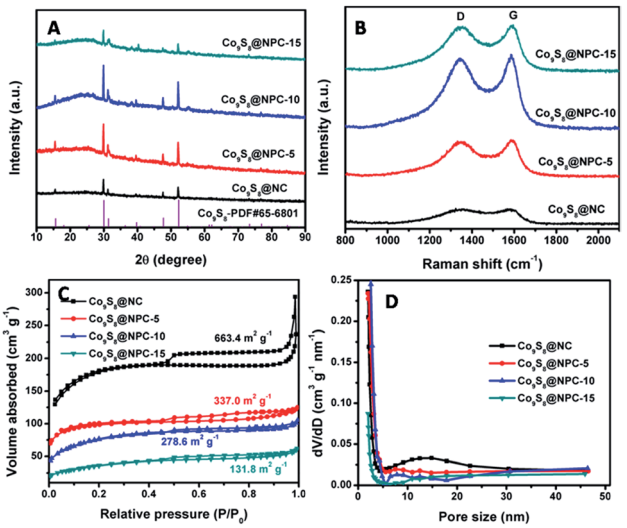


Fig. 2 (A) XRD patterns, (B) Raman spectra, (C) $N_2$ adsorption–desorption isotherms and (D) pore size distribution curves of $Co_9S_8$@NPC-5, $Co_9S_8$@NPC-10, $Co_9S_8$@NPC-15 and $Co_9S_8$@NC.

spectra of all the investigated samples. As shown in Fig. 2B, all the samples' Raman spectra exhibit Raman bands related to carbon structures, including D and G bands. The integrated peak intensity ratio of the D to the G band ($I_D/I_G$) is usually used as a measure of the amount of structural defects and disorder in graphitic carbon structures.[45] The $I_D/I_G$ value of $Co_9S_8$@NC (0.91) is lower than those of $Co_9S_8$@NPC-5 (0.92), $Co_9S_8$@NPC-10 (0.98) and $Co_9S_8$@NPC-15 (1.00), revealing that the level of defects in the graphitic carbon structure increases after phosphidation, resulting from the effect of P doping. Simultaneously, the above Raman analysis also implies that P doping in the graphitic carbon structure could create more catalytically active sites for improving the electrocatalytic activity of the catalyst.[46] The surface areas of the as-prepared samples were measured using the Brunauer–Emmett–Teller (BET) method. As shown in Fig. 2C, a relatively high surface area of 663.4 $m^2\ g^{-1}$ was achieved for the $Co_9S_8$@NC sample, which decreases to 337.0 $m^2\ g^{-1}$ for $Co_9S_8$@NPC-5, 278.6 $m^2\ g^{-1}$ for $Co_9S_8$@NPC-10 and 131.8 $m^2\ g^{-1}$ for $Co_9S_8$@NPC-15. Obviously, the surface area of $Co_9S_8$@NC decreases after phosphidation, and moreover, the $Co_9S_8$@NPC sample's surface area further decreases upon increasing the P doping content, possibly owing to damage to the porous structure of the sample during P doping. To further confirm this, pore structure analysis was performed on all the investigated samples, and the pore size distribution curves of all samples were plotted using the Barrett–Joyner–Halenda (BJH) method. As shown in Fig. 2D, $Co_9S_8$@NC clearly exhibits microporous and mesoporous structures, contributing to the material's high surface area. After phosphidation, the mesopore content is obviously decreased compared to $Co_9S_8$@NC, suggesting possible pore structure damage to the sample during P doping. Even so, a $Co_9S_8$@NPC sample with a porous structure is still favourable for electrocatalysis-related mass transport to improve the electrocatalytic activity when it is used as an electrocatalyst. Comparatively, a P-doped $Co_9S_8$@NC sample fabricated using shrimp-shell derived N-doped carbon nanodots as a carbon and nitrogen source in the presence of $CoSO_4$ without the addition of NaCl–KCl (taking $Co_9S_8$@NPC-10 without NaCl–KCl as an example) exhibits a significantly decreased surface area (49.8 $m^2\ g^{-1}$) and only a microporous structure, implying the significant pore-creating role of the molten-salt calcination approach (Fig. S1B, ESI†). The decreased surface area of this sample could be very unfavourable for its electrocatalytic activity.

To obtain detailed information on the elemental compositions and surface chemical states of the samples, X-ray photoelectron spectroscopy (XPS) analysis was performed. Fig. 3A shows the XPS survey spectrum of $Co_9S_8$@NPC-10, and six elements including Co, S, C, N, P and O can be detected. The O signal should be attributed to the absorbed oxygen species or the residual oxygen-containing groups in the sample. The C and N signals should come from the shrimp-shell derived N-doped carbon nanodots, whereas the P signal is ascribed to the sample post-phosphorization. In the high resolution C 1s spectrum (Fig. 3B), the C 1s peak can be deconvoluted into several parts, corresponding to C–C (284.6 eV), C–N (285.1 eV), C–O (286.1 eV) and C=O (289.0 eV), suggesting N doping in the carbon matrix. For the high resolution N 1s XPS spectrum (Fig. 3C), the N 1s peak can be deconvoluted into four peaks, corresponding to pyridinic N (398.5 eV), pyrrolic N (400.0 eV),

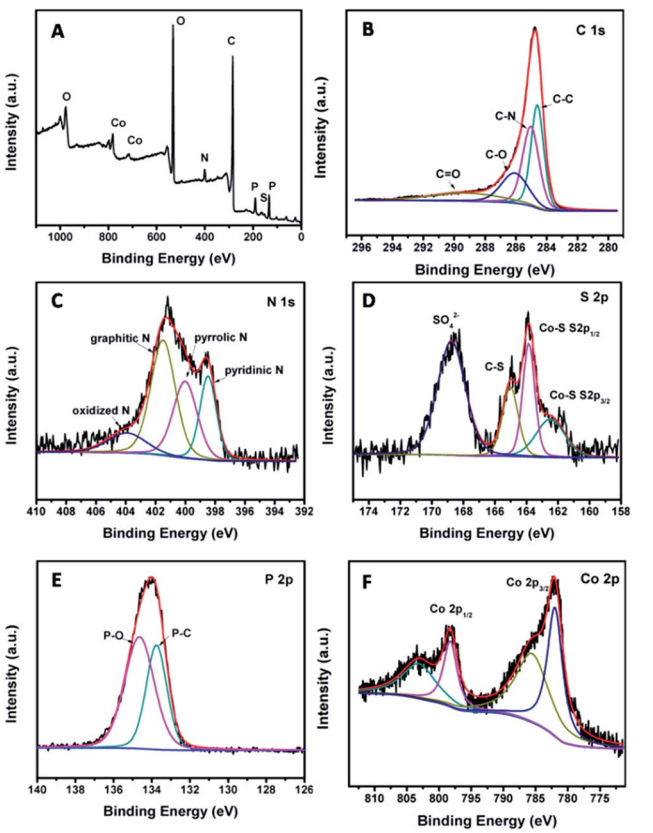


Fig. 3 (A) XPS survey spectrum of $Co_9S_8$@NPC-10. High-resolution spectra of (B) C 1s, (C) N 1s, (D) S 2p, (E) P 2p and (F) Co 2p of $Co_9S_8$@NPC-10.

graphitic N (401.5 eV), and oxidized N (403.9 eV), further indicating N doping in the graphitic carbon structure. Fig. 3D shows the high-resolution S 2p XPS spectrum for $Co_9S_8$@NPC-10. In the S 2p XPS spectrum, the raw curve can be peak-fitted into four curves attributed to three different types of sulfur species. The peaks at 161.4 eV and 162.5 eV can be assigned to the S $2p_{3/2}$ and S $2p_{1/2}$ binding energies of $S^{2-}$ in $Co_9S_8$, respectively, and the peaks at 163.5 eV and 168.4 eV are attributed to C–S and $SO_4^{2-}$, respectively. The existence of C–S could originate from the interfaces between $Co_9S_8$ and the carbon matrix, whereas $SO_4^{2-}$ arose from partly oxidized sulfur species or residual sulfate groups on the surface of the material. The high resolution P 2p XPS spectrum shown in Fig. 3E can be fitted to two peaks: one peak at 132.9 eV is ascribed to P–C bonds, and the other peak at 134.3 eV is due to P–O bonds. The presence of P–C species demonstrates P doping in the graphitic carbon structure after phosphorization. Fig. 3F shows the deconvoluted Co 2p XPS spectrum of $Co_9S_8$@NPC-10 with two main peaks and two satellite peaks. The first main peak, centered at 781.9 eV, is attributed to Co $2p_{3/2}$ ($Co^{2+}$) and its corresponding satellite peak at 785.5 eV is assigned to a mixture of $Co^{2+}$ and $Co^{3+}$. The other main peak at 798.2 eV is assigned to Co $2p_{1/2}$ ($Co^{2+}$) and its corresponding satellite peak is centered at 803.1 eV (also a mixture of $Co^{2+}$ and $Co^{3+}$). Similar results can be also obtained for $Co_9S_8$@NPC-5 and $Co_9S_8$@NPC-15. Moreover, the relative N doping content (Table S1, ESI†) decreases from 5.74% for $Co_9S_8$@NC to 4.38% for $Co_9S_8$@NPC-5, 4.31% for $Co_9S_8$@NPC-10, and 4.28% for $Co_9S_8$@NPC-15 after P doping. Meanwhile, the main nitrogen species in $Co_9S_8$@NPC-10 is graphitic N, which may have a synergy with the doped P in the graphitic carbon structure in terms of improving the electrocatalytic activity of the electrocatalyst. Also, it is found that the P doping content increases from 4.88% for $Co_9S_8$@NPC-5 to 6.51% for $Co_9S_8$@NPC-10 and 7.41% for $Co_9S_8$@NPC-15. Recently, several studies have revealed that N,P co-doped carbon materials (*e.g.*, porous carbon foams, graphene/single-walled carbon nanotubes) can be used as bifunctional electrocatalysts for high performance ORR and OER applications.[47] Further studies have also indicated that the N,P co-doping of carbon materials used as electrocatalysts can effectively improve their hydrogen evolution capability for water splitting in acidic media,[46,48] however there are few reports on these materials as HER electrocatalysts in alkaline media. In this study, N,P co-doped graphitic carbon coupled with a $Co_9S_8$ active species could be used as an electrocatalyst for the HER in an alkaline medium.

To evaluate the electrocatalytic HER activity of the as-prepared materials, the obtained electrocatalyst samples were loaded onto glassy carbon (GC) electrodes and measurements were performed in a 1.0 M KOH solution using a typical three-electrode setup. For comparison, a commercial Pt/C catalyst was also tested with the same loading amount. Before all the measurements, cyclic voltammogram (CV) tests were first performed for 20 cycles in order to stabilize the catalyst. In addition, polarization curves were taken at a scan rate of 5.0 mV $s^{-1}$. Fig. 4A shows the polarization curves of $Co_9S_8$@NC, $Co_9S_8$@NPC-5, $Co_9S_8$@NPC-10, $Co_9S_8$@NPC-15 and Pt/C with *iR* compensation. As shown, the Pt/C catalyst exhibits the highest

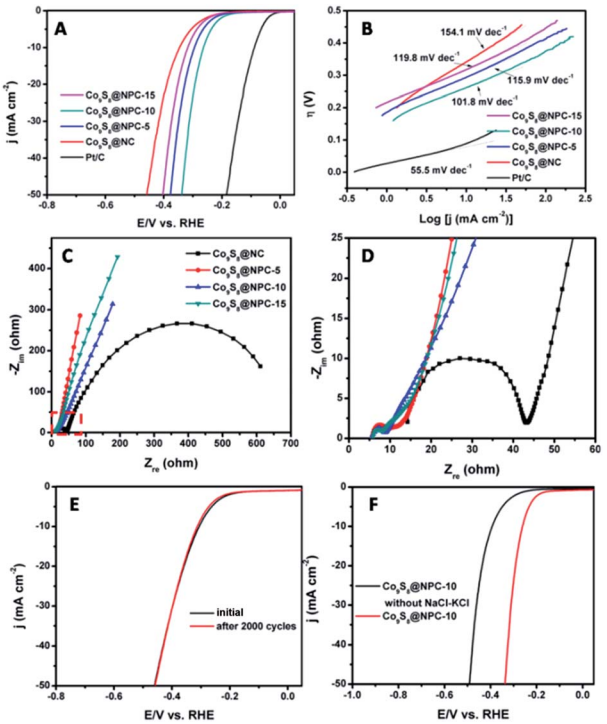


Fig. 4 (A) HER polarization curves for $Co_9S_8$@NPC-5, $Co_9S_8$@NPC-10, $Co_9S_8$@NPC-15, $Co_9S_8$@NC and Pt/C at 5.0 mV $s^{-1}$ in 1.0 M KOH. (B) Corresponding Tafel plots for $Co_9S_8$@NPC-5, $Co_9S_8$@NPC-10, $Co_9S_8$@NPC-15, $Co_9S_8$@NC and Pt/C. (C and D) EIS Nyquist curves for $Co_9S_8$@NPC-5, $Co_9S_8$@NPC-10, $Co_9S_8$@NPC-15 and $Co_9S_8$@NC obtained by applying a sine wave with an amplitude of 5.0 mV over the frequency range from $10^{-1}$ to $10^6$ Hz, where the enclosed area of (C) is magnified in (D). (E) LSV curves for $Co_9S_8$@NPC-10 before and after 2000 CV cycles from −0.3 to +0.2 V at 50 mV $s^{-1}$. (F) HER polarization curves for electrodes of $Co_9S_8$@NPC-10 and $Co_9S_8$@NPC-10 without NaCl–KCl at a scan rate of 5.0 mV $s^{-1}$ in 1.0 M KOH.

HER catalytic activity with a large current density at a lower overpotential and an onset potential close to zero (*vs.* RHE). Apparently, the $Co_9S_8$@NPC samples exhibit better HER catalytic activities than the $Co_9S_8$@NC sample, indicating the significant role of P doping in the graphitic carbon structure in improving the HER activity in alkaline media. Compared to other catalysts, $Co_9S_8$@NPC-10 shows a smaller onset potential of 150 mV (*vs.* RHE). Furthermore, $Co_9S_8$@NPC-10 exhibits an overpotential of 261 mV at a current density of 10 mA $cm^{-2}$, which is obviously smaller than those of $Co_9S_8$@NPC-5 (296 mV), $Co_9S_8$@NPC-15 (318 mV) and $Co_9S_8$@NC (343 mV). For comparison, we measured the HER performance of N-doped porous carbon (NC) and N,P co-doped porous carbon (NPC) fabricated under similar conditions to the $Co_9S_8$@NPC synthesis. As shown in Fig. S2 (ESI†), $Co_9S_8$@NC shows better HER performance than NC, possibly meaning that $Co_9S_8$ is responsible for the improved HER activity.[29,35] Further-improved HER activity is achieved with $Co_9S_8$@NPC-10 compared to $Co_9S_8$@NC, possibly suggesting that appropriate P doping and $Co_9S_8$ in the graphitic carbon structure synergistically enhance the HER activity of the composite in alkaline media. However, excess P doping may result in damage to the

graphitic carbon structure, which is unfavourable for HER activity. A Tafel slope can reflect the inherent properties of an electrocatalyst, and it is always correlated with the reaction pathway and the adsorption type. Therefore, a Tafel slope can be used for quantitative kinetic analysis of the HER. Normally, the linear portions of Tafel plots fit well with the Tafel equation ($\eta = b\log(j) + a$, where $\eta$ is the overpotential, $j$ is the current density, and $b$ is the Tafel slope). Tafel plots for as-prepared samples and the commercial Pt/C catalyst, derived from the polarization curves, are shown in Fig. 4B. The values of the Tafel slopes are 154.1, 115.9, 101.8, 119.8 and 55.5 mV $dec^{-1}$ for $Co_9S_8$@NC, $Co_9S_8$@NPC-5, $Co_9S_8$@NPC-10, $Co_9S_8$@NPC-15 and Pt/C, respectively. Except for the commercial Pt/C catalyst, $Co_9S_8$@NPC-10 exhibits the smallest Tafel slope value, suggesting a faster increment of the HER rate upon increasing the overpotential. To further investigate the interfacial interactions and electrode kinetics of the samples during the HER process, electrochemical impedance spectroscopy (EIS) tests were conducted for the samples with an AC amplitude of 5.0 mV in 1.0 M KOH solution. Fig. 4C shows the Nyquist plots for the catalyst sample loaded electrodes under catalytic HER operating conditions. The ohmic series resistance ($R_S$) was fitted by the intercept of the semicircle on the real axis and the charge transfer resistance ($R_{ct}$) was assigned to the semicircle of the Nyquist plot in terms of the equivalent circuit model. As shown in Fig. 4D, it can be found that the $R_S$ and $R_{ct}$ values of $Co_9S_8$@NPC samples are both less than those of $Co_9S_8$@NC. As is known to all, the $R_S$ provides information about the electrical transport properties of an electrocatalyst, and the $R_{ct}$ is related to the electrocatalytic kinetics at the catalyst/electrolyte interface. Therefore, the above results suggest that the $Co_9S_8$@NPC catalysts have better electrical conductivity and more favorable HER kinetics at the electrode/electrolyte interface in comparison with the $Co_9S_8$@NC catalyst. The long-term use stability of an electrocatalyst is very important for its practical applications in some renewable energy technologies, and therefore we performed a stability test using $Co_9S_8$@NPC-10 as a HER electrocatalyst. As shown in Fig. 4E, after continuously running 2000 cycles of CV measurements from −0.3 V to +0.2 V at 50 mV $s^{-1}$, the LSV curve for the $Co_9S_8$@NPC-10 catalyst still shows a low onset potential similar to the initial potential value, while the current density is slightly reduced after 2000 continuous cycles, indicating its good durability for applications. To confirm the significant role of the molten-salt calcination approach in improving a catalyst's HER performance, we also measured the HER performance of $Co_9S_8$@NPC-10 without the addition of NaCl–KCl during pyrolysis, as shown in Fig. 4F. Obviously, $Co_9S_8$@NPC-10 with its high surface area (278.6 $m^2$ $g^{-1}$) and porous structure exhibits much better HER performance than $Co_9S_8$@NPC-10 without NaCl–KCl, further indicating the important role of the molten-salt calcination approach in creating a porous structure to improve the material's surface area, for the exposure of the catalytic active sites and HER-related mass transport.[6,47]

The development of carbon-based electrocatalysts for water splitting to generate $H_2$ has attracted great attention in recent studies.[1,49,50] However, the $H_2$ generation efficiency is usually limited by the performance of the counterpart oxygen evolution electrode, which has sluggish reaction kinetics during water splitting.[9,10,51,52] Therefore, although water splitting to generate $O_2$ is not very significant compared to generating $H_2$, it is critically important to develop a high efficiency oxygen evolution electrocatalyst with a low overpotential to effectively and efficiently promote $H_2$ generation during electrocatalytic water splitting. Recently reported studies have demonstrated that N,P co-doped carbon materials possess bifunctional electrocatalytic activity toward the oxygen reduction reaction (ORR) and oxygen evolution reaction (OER), exhibiting great potential for applications in rechargeable Zn-air batteries.[47] In this study, we also evaluated the OER activities of the as-prepared catalysts using a three-electrode system in an alkaline electrolyte (1.0 M KOH). As shown in Fig. 5A, it can be seen that all of the catalysts investigated exhibit a similar onset potential (1.53 V *vs.* RHE). At a current density of 10 mA $cm^{-2}$, the OER overpotential values are 400, 410, 403 and 401 mV for $Co_9S_8$@NC, $Co_9S_8$@NPC-5, $Co_9S_8$@NPC-10 and $Co_9S_8$@NPC-15, respectively. For comparison purposes, we also measured the OER performance of NC and NPC samples (Fig. S3, ESI†). As shown, the NC and NPC samples all exhibit very poor OER activities in the alkaline medium, implying the ineffectiveness of performing N,P doping of graphitic carbon structures. This is different to the recently reported results. However, high and similar OER activities can be obtained from the $Co_9S_8$@NC and $Co_9S_8$@NPC-10 samples, possibly indicating that $Co_9S_8$ should be responsible for the high OER activity of the electrocatalyst whether P doped or not.[43] Owing to the bifunctional OER/HER activity of the $Co_9S_8$@NPC sample, we made a device for full water splitting to generate $H_2$ and $O_2$ in an alkaline medium using $Co_9S_8$@NPC concurrently as both the anode and cathode material (taking

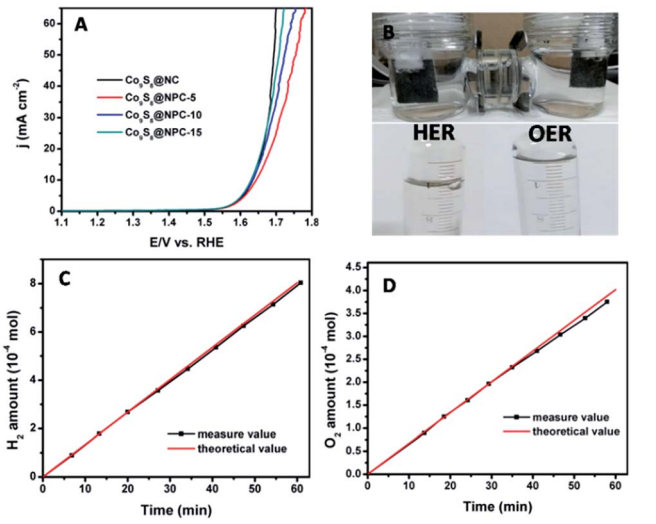


Fig. 5 (A) OER polarization curves for $Co_9S_8$@NPC-5, $Co_9S_8$@NPC-10, $Co_9S_8$@NPC-15 and $Co_9S_8$@NC electrodes at 10 mV $s^{-1}$ in 1.0 M KOH. (B) A photograph of overall water splitting and the gas collection equipment. (C and D) The dependence of the theoretically calculated and experimentally measured hydrogen and oxygen amounts on time during electrocatalytic water splitting using $Co_9S_8$@NPC-10.

$Co_9S_8$@NPC-10 as an example). Fig. 5B shows a photograph of the overall water splitting with obvious gas bubble release, and the gas generated was collected by a simple drainage method. At an applied potential of 1.6 V (corresponding to an overpotential of 370 mV *vs.* RHE), the experimentally measured $H_2$ and $O_2$ generation data fit well with the theoretically calculated ones (Fig. 5C and D). The experimentally measured $H_2$ and $O_2$ generation efficiencies are 13.4 μmol $min^{-1}$ and 6.6 μmol $min^{-1}$, respectively. The faradaic efficiency of $Co_9S_8$@NPC-10 was calculated by comparing the amount of measured gas with the calculated values. A nearly 100% faradaic yield for the HER and OER during alkaline water splitting can be achieved, as shown in Fig. 5C and D. The above results demonstrate the great potential for the application of this biomass-derived carbon material combined with $Co_9S_8$, with N,P co-doping of the active species, for overall water splitting to generate $H_2$ and $O_2$.

## Conclusions

In summary, we successfully synthesized $Co_9S_8$@N,P co-doped porous carbon ($Co_9S_8$@NPC) materials by a combined method using a facile molten-salt calcination approach and post-phosphorization, using shrimp-shell derived carbon nanodots as a carbon and nitrogen source. The experimental results demonstrated that after phosphorization, the samples exhibited decreased surface areas, but significantly improved HER activity in an alkaline medium compared to the samples before phosphorization. Although P doping in a graphitic carbon structure with an appropriate doping amount was confirmed to be favourable for the HER activity of a sample, P doping was found to be ineffective at improving the OER activity of a sample in comparison with the sample before phosphorization. Owing to its bifunctional catalytic activity toward the HER and OER, the $Co_9S_8$@NPC sample was concurrently used as an anode and cathode material for overall water splitting to generate $H_2$ and $O_2$, exhibiting a nearly 100% faradic yield in an alkaline medium. The strategy developed in this study provides an efficient approach to fabricate non-precious metal bifunctional HER/OER electrocatalysts for full water splitting to generate $H_2$ and $O_2$ using low-cost and abundant biomass as a staring material.

## Acknowledgements

This work was financially supported by the Natural Science Foundation of China (Grant No. 51672277 and 51372248), the CAS Pioneer Hundred Talents Program and the CAS/SAFEA International Partnership Program for Creative Research Teams of the Chinese Academy of Sciences, China.

## Notes and references

1 X. X. Zou and Y. Zhang, *Chem. Soc. Rev.*, 2015, **44**, 5148–5180.
2 B. Rausch, M. D. Symes, G. Chisholm and L. Cronin, *Science*, 2014, **345**, 1326–1330.
3 H. Y. Li, Q. W. Tang, B. L. He and P. Z. Yang, *J. Mater. Chem. A*, 2016, **4**, 6513–6520.
4 J. Xu, J. B. Cui, C. Guo, Z. P. Zhao, R. Jiang, S. Y. Xu, Z. B. Zhuang, Y. Huang, L. Y. Wang and Y. D. Li, *Angew. Chem., Int. Ed.*, 2016, **55**, 6502–6505.
5 S. M. Tan and M. Pumera, *ACS Appl. Mater. Interfaces*, 2016, **8**, 3948–3957.
6 X. H. Zhu, M. J. Liu, Y. Liu, R. W. Chen, Z. Nie, J. H. Li and S. Z. Yao, *J. Mater. Chem. A*, 2016, **4**, 8974–8977.
7 J. Durst, C. Simon, F. Hasche and H. A. Gasteiger, *J. Electrochem. Soc.*, 2015, **162**, F190–F203.
8 A. R. J. Kucernak and V. N. N. Sundaram, *J. Mater. Chem. A*, 2014, **2**, 17435–17445.
9 K. Yin, Z. D. Cui, X. R. Zheng, X. J. Yang, S. L. Zhu, Z. Y. Li and Y. Q. Liang, *J. Mater. Chem. A*, 2015, **3**, 22770–22780.
10 X. Zhang, R. R. Liu, Y. P. Zang, G. Q. Liu, G. Z. Wang, Y. X. Zhang, H. M. Zhang and H. J. Zhao, *Chem. Commun.*, 2016, **52**, 5946–5949.
11 C. G. Read, J. F. Callejas, C. F. Holder and R. E. Schaak, *ACS Appl. Mater. Interfaces*, 2016, **8**, 12798–12803.
12 W. W. Guo, H. J. Lv, Z. Y. Chen, K. P. Sullivan, S. M. Lauinger, Y. N. Chi, J. M. Sumliner, T. Q. Lian and C. L. Hill, *J. Mater. Chem. A*, 2016, **4**, 5952–5957.
13 G. F. Wei and Z. P. Liu, *Chem. Sci.*, 2015, **6**, 1485–1490.
14 K. Elbert, J. Hu, Z. Ma, Y. Zhang, G. Y. Chen, W. An, P. Liu, H. S. Isaacs, R. R. Adzic and J. X. Wang, *ACS Catal.*, 2015, **5**, 6764–6772.
15 L. Wang, E. G. Mahoney, S. Zhao, B. Yang and J. G. G. Chen, *Chem. Commun.*, 2016, **52**, 3697–3700.
16 Y. M. Yang, J. Liu, S. J. Guo, Y. Liu and Z. H. Kang, *J. Mater. Chem. A*, 2015, **3**, 18598–18604.
17 N. Jiang, Q. Tang, M. L. Sheng, B. You, D. E. Jiang and Y. J. Sun, *Catal. Sci. Technol.*, 2016, **6**, 1077–1084.
18 M. Gong, D. Y. Wang, C. C. Chen, B. J. Hwang and H. J. Dai, *Nano Res.*, 2016, **9**, 28–46.
19 Y. P. Liu, G. D. Li, L. Yuan, L. Ge, H. Ding, D. J. Wang and X. X. Zou, *Nanoscale*, 2015, **7**, 3130–3136.
20 L. B. Ma, Y. Hu, R. P. Chen, G. Y. Zhu, T. Chen, H. L. Lv, Y. R. Wang, J. Liang, H. X. Liu, C. Z. Yan, H. F. Zhu, Z. X. Tie, Z. Jin and J. Liu, *Nano Energy*, 2016, **24**, 139–147.
21 Z. H. Pu, Q. Liu, A. M. Asiri, Y. L. Luo, X. P. Sun and Y. Q. He, *Electrochim. Acta*, 2015, **168**, 133–138.
22 X. H. Xia, Z. X. Zheng, Y. Zhang, X. J. Zhao and C. M. Wang, *Int. J. Hydrogen Energy*, 2014, **39**, 9638–9650.
23 X. M. Geng, W. Wu, N. Li, W. W. Sun, J. Armstrong, A. Al-hilo, M. Brozak, J. B. Cui and T. P. Chen, *Adv. Funct. Mater.*, 2014, **24**, 6123–6129.
24 L. Yang, M. G. Gao, B. Dai, X. H. Guo, Z. Y. Liu and B. H. Peng, *Electrochim. Acta*, 2016, **191**, 813–820.
25 W. X. Zhu, X. Y. Yue, W. T. Zhang, S. X. Yu, Y. H. Zhang, J. Wang and J. L. Wang, *Chem. Commun.*, 2016, **52**, 1486–1489.
26 D. Y. Chung, J. W. Han, D. H. Lim, J. H. Jo, S. J. Yoo, H. Lee and Y. E. Sung, *Nanoscale*, 2015, **7**, 5157–5163.
27 D. Jasion, J. M. Barforoush, Q. Qiao, Y. M. Zhu, S. Q. Ren and K. C. Leonard, *ACS Catal.*, 2015, **5**, 6653–6657.

28 H. C. Zhang, Y. J. Li, G. X. Zhang, P. B. Wan, T. H. Xu, X. C. Wu and X. M. Sun, *Electrochim. Acta*, 2014, **148**, 170–174.
29 L. L. Feng, M. H. Fan, Y. Y. Wu, Y. P. Liu, G. D. Li, H. Chen, W. Chen, D. J. Wang and X. X. Zou, *J. Mater. Chem. A*, 2016, **4**, 6860–6867.
30 N. Zhang, W. G. Ma, F. Jia, T. S. Wu, D. X. Han and L. Niu, *Int. J. Hydrogen Energy*, 2016, **41**, 3811–3819.
31 S. Reddy, R. Du, L. X. Kang, N. N. Mao and J. Zhang, *Appl. Catal., B*, 2016, **194**, 16–21.
32 Y. R. Liu, W. H. Hu, X. Li, B. Dong, X. Shang, G. Q. Han, Y. M. Chai, Y. Q. Liu and C. G. Liu, *Appl. Surf. Sci.*, 2016, **384**, 51–57.
33 S. J. Peng, L. L. Li, X. P. Han, W. P. Sun, M. Srinivasan, S. G. Mhaisalkar, F. Y. Cheng, Q. Y. Yan, J. Chen and S. Ramakrishna, *Angew. Chem., Int. Ed.*, 2014, **53**, 12594–12599.
34 T. Y. Wang, L. Liu, Z. W. Zhu, P. Papakonstantinou, J. B. Hu, H. Y. Liu and M. X. Li, *Energy Environ. Sci.*, 2013, **6**, 625–633.
35 L. L. Feng, G. D. Li, Y. Liu, Y. Wu, H. Chen, Y. Wang, Y. C. Zou, D. Wang and X. Zou, *ACS Appl. Mater. Interfaces*, 2015, **7**, 980–988.
36 X. Zhang, R. R. Liu, Y. P. Zang, G. Q. Liu, S. W. Liu, G. Z. Wang, Y. X. Zhang, H. M. Zhang and H. J. Zhao, *Inorg. Chem. Front.*, 2016, **3**, 910–918.
37 X. Deng, B. Zhao, L. Zhu and Z. Shao, *Carbon*, 2015, **93**, 48–58.
38 B. He, W.-C. Li and A.-H. Lu, *J. Mater. Chem. A*, 2015, **3**, 579–585.
39 R. R. Liu, H. M. Zhang, S. W. Liu, X. Zhang, T. X. Wu, X. Ge, Y. P. Zang, H. J. Zhao and G. Z. Wang, *Phys. Chem. Chem. Phys.*, 2016, **18**, 4095–4101.
40 W. Liu, E. Hu, H. Jiang, Y. Xiang, Z. Weng, M. Li, Q. Fan, X. Yu, E. I. Altman and H. Wang, *Nat. Commun.*, 2016, **7**, 10771.
41 M. Caban-Acevedo, M. L. Stone, J. R. Schmidt, J. G. Thomas, Q. Ding, H. C. Chang, M. L. Tsai, J. H. He and S. Jin, *Nat. Mater.*, 2015, **14**, 1245–1251.
42 Y. Pan, Y. Liu and C. Liu, *Appl. Surf. Sci.*, 2015, **357**, 1133–1140.
43 S. Dou, L. Tao, J. Huo, S. Wang and L. Dai, *Energy Environ. Sci.*, 2016, **9**, 1320–1326.
44 Y. B. Li, H. M. Zhang, Y. Wang, P. R. Liu, H. G. Yang, X. D. Yao, D. Wang, Z. Y. Tang and H. J. Zhao, *Energy Environ. Sci.*, 2014, **7**, 3720–3726.
45 J. J. Duan, S. Chen, M. Jaroniec and S. Z. Qiao, *ACS Nano*, 2015, **9**, 931–940.
46 Y. Zheng, Y. Jiao, L. H. Li, T. Xing, Y. Chen, M. Jaroniec and S. Z. Qiao, *ACS Nano*, 2014, **8**, 5290–5296.
47 J. T. Zhang, L. T. Qu, G. Q. Shi, J. Y. Liu, J. F. Chen and L. M. Dai, *Angew. Chem., Int. Ed.*, 2016, **55**, 2230–2234.
48 D. F. Yan, S. Dou, L. Tao, Z. J. Liu, Z. G. Liu, J. Huo and S. Y. Wang, *J. Mater. Chem. A*, 2016, **4**, 13726–13730.
49 S. Y. Guo and S. Han, *J. Power Sources*, 2014, **267**, 9–13.
50 J. Swaminathan, R. Subbiah and V. Singaram, *ACS Catal.*, 2016, **6**, 2222–2229.
51 M. Ledendecker, G. Clavel, M. Antonietti and M. Shalom, *Adv. Funct. Mater.*, 2015, **25**, 393–399.
52 Y. Y. Wang, D. D. Liu, Z. J. Liu, C. Xie, J. Huo and S. Y. Wang, *Chem. Commun.*, 2016, **52**, 12614–12617.